Rev. Roum. Sci. Techn.– Électrotechn. et Énerg.
Vol. **71**, *4*, pp. 519–524, Bucarest, 2026

DATASHEET-CONSTRAINED MODELING OF SATELLITE PHOTOVOLTAIC ELECTRICAL POWER SUBSYSTEM UNDER AM0 CONDITIONS

AICHA MELIT[1,2], AISSA MEFLAH[1], KARIM KEMIH[2]

Keywords: CubeSat electrical power subsystem (EPS); Orbital energy modeling; Maximum power point tracking (MPPT); DC-DC topology; Battery state of charge.

This paper formalizes a modeling methodology for satellite photovoltaic electrical power subsystem (EPS) studies under datasheet-only constraints. The proposed framework couples a two-diode model, a reduced-order 3J equivalent space surrogate, orbital dynamics, and EPS components into a unified simulation chain. Using the three official datasheet references for strict consistency assessment, the 3J Equivalent surrogate reduces the mean absolute Pmax and Vmp errors to 0.07 % and 0.09 %, respectively, compared with 2.86 % and 4.00 % for the two-diode baseline. In a representative low earth orbit (LEO) mission scenario for the GomSpace DSP baseline, the Incremental Conductance (INC) algorithm achieves the highest energy retention, while the boost converter topology achieves a PV-to-bus delivery ratio of 94.41 %.

1. INTRODUCTION

Satellite missions, especially CubeSat and nanosatellite missions, are strongly constrained by the limited electrical energy that can be generated, conditioned, stored, and dispatched during alternating sunlit and eclipse phases. The restricted collecting area, rapid temperature changes, mission-dependent load peaks, and battery charging constraints make the electrical power subsystem (EPS) one of the dominant drivers of mission energy margin and payload availability. In that context, improving satellite photovoltaic performance is not limited to cell efficiency alone; it also requires the integrated analysis of the generator, the tracking algorithm, the DC-DC stage, the battery, and the time-dependent mission load.

Unlike terrestrial photovoltaic studies, which are commonly referenced to standard test conditions (STC), space photovoltaic studies must be formulated under air mass zero (AM0) conditions. They must also use the specific terminology of solar cells, solar cell assemblies, and photovoltaic assemblies defined in space standards. This distinction is not merely formal; it directly affects the spectral assumptions, temperature references, radiation-induced degradation treatment, and the interpretation of manufacturer data. For this reason, the present study adopts an explicitly AM0-centered formulation and is fully aligned with ECSS terminology and mission framing throughout the manuscript [1]. Recent studies published in this journal have addressed microgrid optimization [2], ANFIS-based maximum power point tracking (MPPT) implementation [3], and MPPT techniques for nanosatellite power systems [4], confirming the growing interest in simulation-based design tools for renewable and aerospace power systems.

The absence of experimental access to space-qualified cells and panel-level orbital testing platforms is a common constraint in academic feasibility studies and early-phase industrial pre-design, where hardware procurement or thermal-vacuum testing infrastructure may not yet be available [1,5–7]. Within this perspective, the paper develops a unified framework that connects AM0 consistency assessment, thermal-electrical sensitivity, beginning-of-life (BOL) to end-of-life (EOL) analysis, orbital power generation, maximum power point tracking (MPPT) comparison, topology-dependent power conditioning, battery behavior, and mission-load scheduling in a single workflow. Hereafter, this datasheet-constrained framework is denoted DCF. The study is formulated as a system-aware simulation methodology suitable for early-mission EPS design before experimental access becomes available. This integrated viewpoint is consistent with recent thermal-electrical and EPS-oriented studies for small satellites [8–15].

However, to the best of the authors' knowledge, no existing study simultaneously addresses AM0 consistency assessment, multi-algorithm MPPT comparison, and topology-dependent power conditioning within a unified datasheet-only constraint framework for CubeSat EPS applications. This gap motivates the present work. The main contributions of this work are:

- Formalization of a unified AM0-consistent DCF simulation chain under datasheet-only constraints, without experimental hardware access.
- Demonstration that the reduced-order 3J Equivalent Space surrogate improves the official-datasheet V_{mp} error by more than a factor of 40 (from 4.00% to 0.09%).
- Orbit-level MPPT comparison shows that INC achieves 99.18% energy retention while maintaining the highest final state of charge (SOC) of 62.80 %.
- Quantification of DC-DC topology impact: the boost topology delivers 94.41% of PV-side energy to the 28 V bus, whereas the buck case transfers only 42.17% because most of the deficit is source-bus mismatch rather than dissipative converter loss.

The paper is organized as follows: Section 2 presents the reference database and photovoltaic models. Section 3 describes the EPS modeling framework, including orbital dynamics, MPPT strategies, and the battery model. Section 4 reports and discusses the simulation results. Section 5 draws the conclusions.

2. REFERENCE DATABASE AND PHOTOVOLTAIC MODELS

2.1. REFERENCE DATABASE AND SOURCE INTEGRITY

The reference database used in this study combines official standards, official manufacturer documentation, and recent peer-reviewed papers. The standard backbone is provided by the ECSS photovoltaic standard [1]. Cell-level benchmarking anchors are taken from the official Spectrolab XTJ Prime and Sharp IMM3J datasheets [5,6], while the panel-level baseline is supported by the official GomSpace NanoPower DSP datasheet [7]. Public platform and mission

[1] Unité de Développement des Équipements Solaires (UDES), Centre de Développement des Énergies Renouvelables (CDER), 42004 Tipaza, Algeria.
[2] L2EI Laboratory, Mohamed Seddik Benyahia University, Jijel, Algeria.
E-mails: a.melit@cder.dz, a.meflah@cder.dz, karim_kemih@univ-jijel.dz

DOI: 10.59277/RRST-EE.2026.4.7

sources [16–20] , and NASA technology roadmaps [21,22], further confirm the relevance of AM0-centered performance analysis. Additional CubeSat and solar-array references are provided in [23–26].

Table 1
Benchmark photovoltaic devices and source quality.

Device	Level	Technology	Source quality	P_{max} (W)	Efficiency (%)
Spectrolab XTJ Prime Cell	cell	3J	official datasheet	1.149	31.12
Sharp IMM3J Cell	cell	IMM3J	official datasheet	1.156	30.87
GomSpace NanoPower P110	panel	3J	estimated from V_{oc}/I_{sc}	2.408	29.18
GomSpace NanoPower DSP 135deg	panel	3J	official datasheet	21.149	28.65

2.2. EFFECTIVE IRRADIANCE AND THERMAL SENSITIVITY

The effective irradiance G_{eff} incident on the photovoltaic surface is expressed as:

$$G_{eff} = G_{AM0}\cos(\theta) f_{exp}, \quad (1)$$

where G_{AM0} = 1367 W/m² is the extraterrestrial solar irradiance, θ is the incidence angle, and f_{exp} accounts for exposure conditions. The modeling approach is fully aligned with recent mission-scheduling and remote-sensing studies for specialized CubeSats [27–30]. The short-circuit current and open-circuit voltage dependence on temperature and irradiance are given by [31]:

$$I_{sc} = I_{sc,ref}\frac{G}{G_{ref}}\left[1 + \alpha(T - T_{ref})\right], \quad (2)$$

$$V_{oc} = V_{oc,ref} + \beta\left(T - T_{ref}\right) + nV_t \ln\left(\frac{G}{G_{ref}}\right), \quad (3)$$

$$V_t = \frac{kT}{q}, \quad (4)$$

where k is the Boltzmann constant and q is the electron charge. The coefficients α and β are the current and voltage temperature coefficients, respectively.

2.3. PHOTOVOLTAIC MODEL CORES

The electrical behavior of the PV cell is described by the two-diode model:

$$= I_{ph} - I_{01}\left(e^{\frac{V+IR_s}{n_1 V_t}} - 1\right) - I_{02}\left(e^{\frac{V+IR_s}{n_2 V_t}} - 1\right) - \frac{V + IR_s}{R_{sh}}, \quad (5)$$

where I_{ph} is the photogenerated current, I_{01} and I_{02} are dark saturation currents, n_1 and n_2 are ideality factors, R_s is series resistance, and R_{sh} is shunt resistance. A reduced-order empirical model is also adopted. The analytical form of the 3J Equivalent model is given by eq. (6) and calibrated using datasheet corner points (I_{sc}, V_{oc}, V_{mp}, I_{mp}):

$$I(V) = I_{sc}\left(1 - \left(\frac{V}{V_{oc}}\right)^{a_f}\right)^{b_f}, \quad (6)$$

where a_f and b_f are empirical fitting parameters identified from datasheet corner points to reproduce the pronounced knee typical of multi-junction devices [31].

3. EPS MODELING FRAMEWORK

The approach integrates orbital dynamics, power electronics, and energy storage into a unified EPS-level simulation. All simulations were carried out in Python using the NumPy and SciPy libraries.

The orbital period was discretized with a time step of 1 s. The global synoptic workflow is illustrated in Fig. 1.

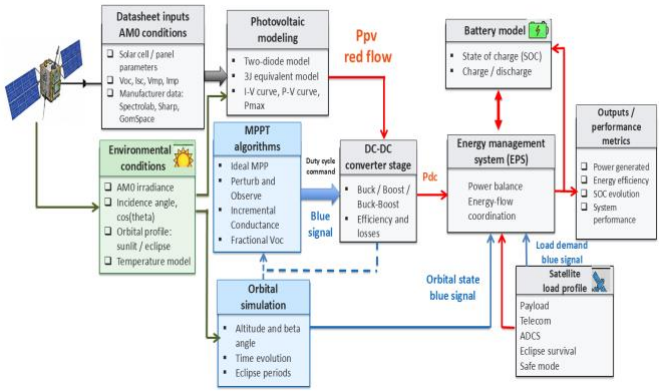


Fig. 1 – Global synoptic workflow of the dataset-constrained simulation framework.

3.1. ORBITAL AND THERMAL BLOCKS

The orbital period T is computed using Kepler's third law [32]:

$$T = 2\pi\sqrt{\frac{(R_E + h)^3}{\mu_E}} \quad (7)$$

where R_E is the Earth radius, h is the altitude, and μ_E is Earth's gravitational parameter. A first-order thermal model is used:

$$T_{k+1} = T_k + a(T_{eq} - T_k) \quad (8)$$

where T_{eq} is the equilibrium temperature combining direct AM0 absorption, Earth albedo, and infrared flux. The thermal time constant τ_{th} is set to 900 s, representing the average thermal inertia of the CubeSat panel.

3.2. MPPT AND POWER CONDITIONING

The MPPT efficiency η_{MPPT} and normalized root mean square error $NRMSE_{MPPT}$ are defined as:

$$\eta_{MPPT} = \frac{E_{alg}}{E_{ideal}}, \#(9)$$

$$NRMSE_{MPPT} = 100\sqrt{\frac{1}{N}\sum_{k=1}^{N}\left(\frac{P_{alg,k} - P_{MPP,k}}{P_{MPP,k}}\right)^2}. \quad (10)$$

Converter losses P_{loss} include conduction, switching, diode, gate-drive, control, and magnetic contributions.

$$P_{loss} = P_{cond} + P_{sw} + P_{diod} + P_{gat} + P_{ctrl} + P_{mag}. \quad (11)$$

For the boost topology, the duty cycle D follows the relationship $V_{bus} = V_{pv}/(1-D)$. Switching losses are particularly important in high-frequency nanosatellite converters [33,34].

3.3. BATTERY STORAGE MODEL

The SOC is computed using an energy-based discrete formulation [35]:

$$SOC_{k+1} = SOC_k + \frac{\eta_{ch}P_{ch} - \frac{P_{dis}}{\eta_{dis}}}{E_{bat}}\Delta t. \quad (12)$$

where η_{ch} and η_{dis} are the charge and discharge efficiencies. Nominal parameters are summarized in Table 2.

Table 2

Nominal DC-DC and orbital simulation parameters.

Symbol	Parameter	Value
V_{bus}	Regulated bus voltage	28 V
P_{rated}	Rated converter power	45 W
f_s	Switching frequency	150 kHz
C_{bat}	Battery capacity	4.2 Ah
η_{ch}	Charge efficiency	0.96
h	Orbital altitude	550 km
β_{orb}	Beta angle	25 °
τ_{th}	Thermal constant	900 s
α_s	Solar absorptivity	0.78
ε	IR emissivity	0.84
ηdis	Discharge efficiency	0.95
SOC0	Initial SOC	82 %

4. RESULTS AND DISCUSSION

4.1. CONSISTENCY ASSESSMENT OF THE ELECTRICAL CORES

A comparative analysis was recalculated using only the three official datasheet references: Spectrolab XTJ Prime, Sharp IMM3J, and GomSpace NanoPower DSP. The partly inferred GomSpace P110 point remains in Table 1 for context but is excluded from Table 3 to avoid circularity. The 3J Equivalent model reduces Pmax MAE from 2.86 % to 0.07% and V_{mp} MAE from 4.00% to 0.09%; Table 3 therefore represents a datasheet-reconstruction consistency assessment rather than an out-of-sample predictive validation.

Table 3

Electrical-core consistency metrics (MAE in %).

Model core	P_{max}	V_{oc}	I_{sc}	V_{mp}	I_{mp}
Two-Diode Space	2.86	0.18	0.09	4.00	1.17
3J Equivalent	0.07	0.00	0.00	0.09	0.09

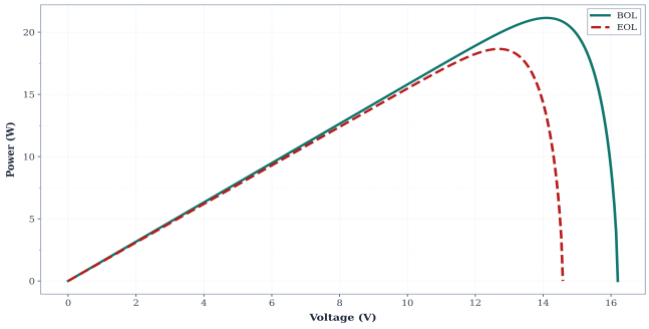


Fig. 2 – BOL/EOL power comparison for the selected photovoltaic devices.

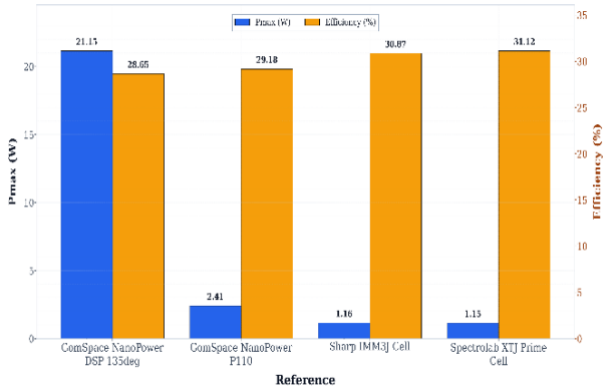


Fig. 3 – Output power and efficiency of the selected benchmark devices.

The 3J Equivalent surrogate reduces the official-datasheet V_{mp} error by more than a factor of 40. For the GomSpace DSP baseline, the Two-Diode implementation uses $I_{01} = I_{02} = 1.39 \cdot 10^{-15}$ A, $n_1 = 1.0$, $n_2 = 1.2$, $R_s = 0.0734$ Ω and $R_{sh} = 246.94$ Ω; the 3J Equivalent fit gives $a_f = 18.483$ and $b_f = 0.650$ from I_{sc}, V_{oc}, V_{mp} and I_{mp}.

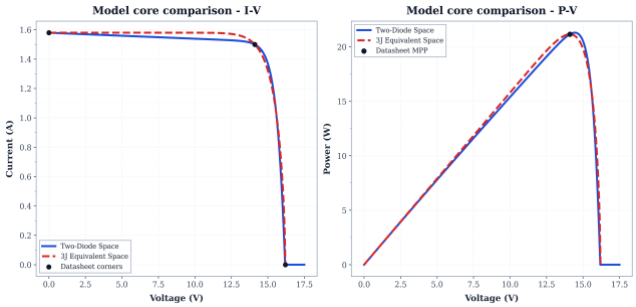


Fig. 4 – Electrical-core comparison for the GomSpace DSP baseline.

Figures 2-4 illustrate the device-level performance. As shown in Fig. 2, the IMM3J cell shows the highest sensitivity to radiation degradation.

4.2. SENSITIVITY ANALYSIS

Increasing temperature from -120 °C to 120 °C reduces Pmax by about 30.6 % for the GomSpace baseline; this is a device-level sensitivity envelope, not the retained 550 km, β = 25° orbital thermal range of –38.6°C to 29.3°C. At 75° incidence, the retained power is 24.9% of the normal-incidence value, corresponding to a 75.1% irradiance-related reduction (Fig. 5).

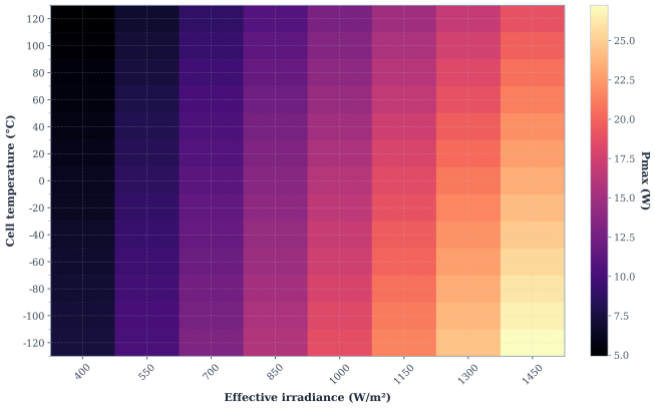


Fig. 5 – P_{max} heatmap showing the combined influence of irradiance and temperature.

4.3. ORBITAL BEHAVIOR AND MPPT COMPARISON

The orbit-level study confirms that INC achieves the highest energy retention (99.18%). Although fractional V_{oc} shows lower $NRMSE_{illum}$ (10.12%), its systematic bias reduces harvested energy (Table 4).

Table 4

MPPT performance metrics under the retained orbital scenario.

MPPT Algorithm	PV-side harvested energy (Wh)	Tracking Eff. (%)	$NRMSE_{illum}$ (%)	Final SOC (%)
Ideal MPP	29.82	100.00	0.00	62.99
Incremental Conductance	29.58	99.18	15.38	62.80
P&O	28.54	95.71	13.71	62.00
Fractional V_{oc}	27.93	93.67	10.12	61.47

The INC algorithm maintains a final SOC of 62.80%, outperforming the Fractional V_{oc} strategy by 2.2% of SOC.

The higher NRMSE of INC does not translate into lower harvested energy in the simulated scenario, indicating that instantaneous tracking error and cumulative energy retention represent distinct performance metrics. Figures 6-8 detail the tracking dynamics.

The MPPT transition behavior was also checked during sunlit-to-eclipse changes. INC keeps the highest PV-side energy retention in this scenario, although its instantaneous NRMSE is not the lowest; therefore, tracking precision and delivered energy should be interpreted as distinct metrics.

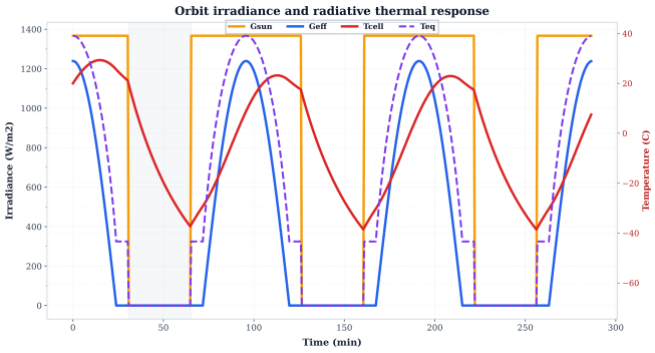


Fig. 6 – Orbital irradiance, thermal trend, and cell temperature over three orbits.

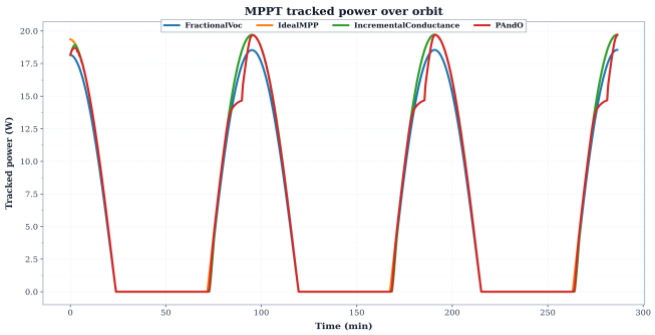


Fig. 7 – Tracked photovoltaic power for the compared MPPT algorithms.

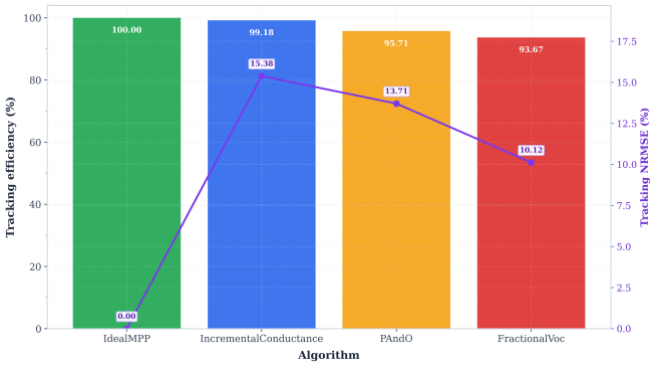


Fig. 8 – Orbit-averaged MPPT tracking efficiency and illuminated-phase NRMSE.

4.4. EPS AND MISSION LOAD INTERPRETATION

The bus-side power remains lower than the raw photovoltaic input by about 0.61 W, on average during active PV operation for the boost case (Fig. 9). The battery ends the simulated window at 62.80% SOC (Fig. 10). Table 4 reports PV-side harvested energy, whereas Fig. 11 reports bus-side delivered energy after DC-DC conversion.

Over the simulated window, eclipse survival accounts for the largest cumulative mission-mode energy demand (15.20 Wh), followed by payload acquisition (12.73 Wh). Figure 11 summarizes the corresponding EPS-level performance across the MPPT algorithms in terms of bus-side delivered energy, PV-to-bus delivery ratio, average converter loss, and final battery SOC.

Table 5

Mission modes, loads, and activation rules.

Mission mode	Average load (W)	Activation rule	Energy (Wh)
nominal_sun	7.6	Default sunlit fallback	8.41
payload_acquisition	12.5	Every 24 min for 10 min	12.73
telecom_downlink	13.7	Every 30 min for 7 min	9.59
eclipse_survival	8.8	Active during eclipse	15.20

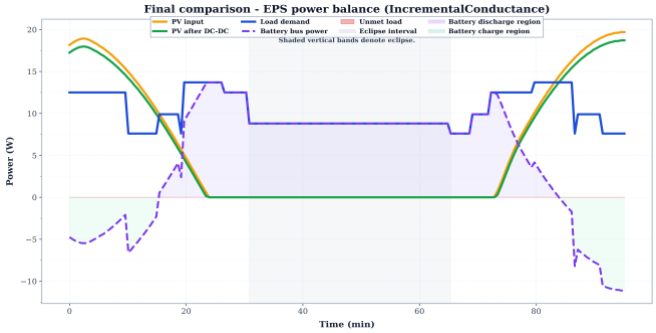


Fig. 9 – EPS power balance over one representative orbit.

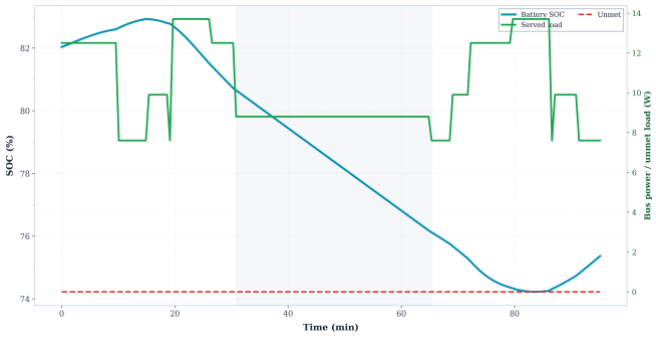


Fig. 10 – Battery state of charge and delivered load timeline.

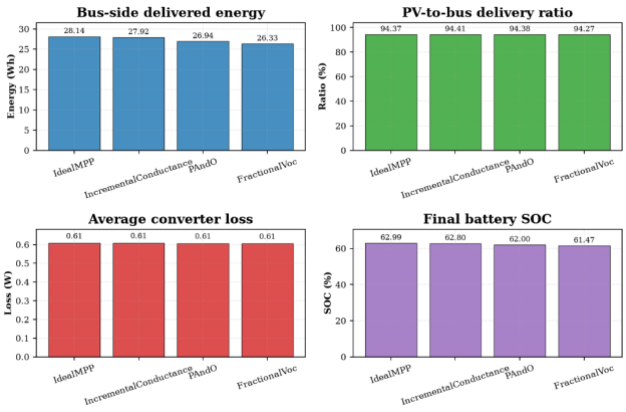


Fig. 11 – Integrated EPS metrics summary by MPPT algorithm.

4.5. DC-DC TOPOLOGY COMPARISON

Topology selection is constrained by source-bus compatibility. For the 28 V bus, the boost topology provides the most effective coupling, with a PV-to-bus delivery ratio

of 94.41%. The buck topology transfers only 42.17% of the PV-side energy because it remains in dropout when the panel voltage is below the regulated bus (Table 6).

Table 6
DC-DC topology performance summary.

DC-DC topology	PV-to-bus (%)	Bus (Wh)	Dissipative loss (Wh)	Source-bus mismatch (Wh)	Final SOC (%)
boost	94.41	27.92	1.43	0.22	62.80
buck-boost	94.10	27.83	1.67	0.08	62.71
buck	42.17	12.47	1.33	15.78	49.59

For all three topology comparisons, the INC reference provides 29.58 Wh of harvestable PV-side energy. The buck case closes as 29.58 Wh = 12.47 Wh delivered to the bus +1.33 Wh dissipative loss +15.78 Wh source-bus mismatch energy, with zero residual at reporting precision. Thus, 42.17% is a PV-to-bus delivery ratio, not an intrinsic dissipative efficiency.

The loss breakdown (Fig. 13) shows comparable active-period average dissipative losses, computed over samples with non-zero PV input power: 0.61 W for boost, 0.71 W for buck-boost, and 0.56 W for buck. The buck deficit is therefore dominated by source-bus incompatibility under the 28 V architecture, whereas boost and buck-boost maintain effective coupling over the illuminated samples.

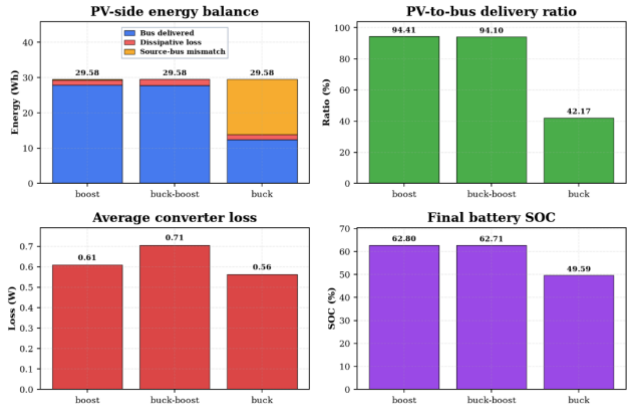


Fig. 12 – Integrated metrics by DC-DC topology.

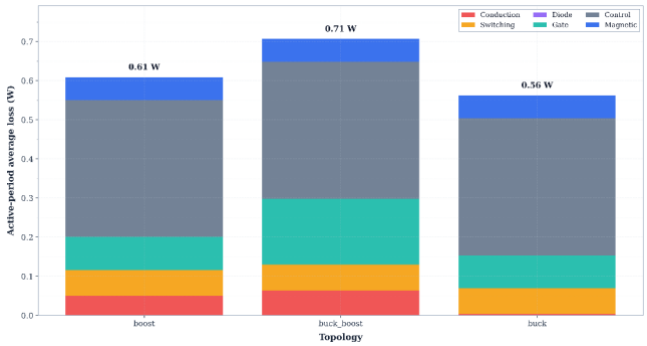


Fig. 13 –Active-period average DC-DC loss breakdown by converter topology.

4.6. INTEGRATED ENERGY-BALANCE DISCUSSION

The transition from cell-level consistency to system-level energy balance confirms that model choice propagates through the simulation chain. The 3J Equivalent model improves voltage reconstruction near the manufacturer performance knee, and INC gives the highest PV-side energy retention in the simulated orbital scenario.

The integrated DCF workflow separates MPPT tracking, DC-DC conversion, battery losses, and mission-load effects. This helps early EPS studies identify whether an energy deficit comes from tracking, conversion loss, storage constraints, or source-bus incompatibility before hardware access is available.

5. CONCLUSION

This study has formalized a comprehensive datasheet-constrained modeling framework (DCF) for satellite photovoltaic EPS analysis. The reduced-order 3J Equivalent Space surrogate gives an official-datasheet V_{mp} MAE of 0.09%. At orbital scale, INC gives the highest PV-side energy retention (99.18%) and maintains a 62.80% final SOC. The DC-DC topology analysis shows that boost is the most appropriate of the tested options for the 28 V bus, achieving a 94.41 % PV-to-bus delivery ratio, while the buck limitation is mainly caused by source-bus mismatch rather than dissipative loss. The broader significance of this research lies in its ability to support satellite engineers with an integrated design-support tool that translates manufacturer datasheet parameters into actionable mission-level insights. By ensuring that cell-level consistency improvements propagate accurately through the EPS simulation chain, the DCF methodology reduces the risks associated with early-stage power budget planning when experimental hardware access is restricted.

Future research directions will focus on extending this framework to multi-mission constellation deployments and integrating complex thermo-optical aging models, particularly those accounting for radiation-induced displacement damage, to support the next generation of long-duration deep-space and LEO missions.

CREDIT AUTHORSHIP CONTRIBUTION

Aicha MELIT: study conception and design; study conception and design; draft manuscript preparation; analysis and interpretation of results; reviewed the results and approved the final version of the manuscript.

Aissa MEFLAH: study conception and design; study conception and design; software; draft manuscript preparation; analysis and interpretation of results; reviewed the results and approved the final version of the manuscript.

Karim KEMIH: draft manuscript preparation; analysis and interpretation of results; reviewed the results and approved the final version of the manuscript.

Received on 4 May 2026

REFERENCES

1. ***ECSS Secretariat, *ECSS-E-ST-20-08C Rev. 2: Space engineering – Photovoltaic assemblies and components*, ESA-ESTEC, Noordwijk, 20 April 2023. Archived PDF: https://escies.org/ftp/ecss.nl/ECSS/ (Active ECSS Standards, PDF archive, 10 Oct. 2025).
2. A. Firah, M. Birane, A. Degla, "Techno-economic based optimization of photovoltaic/battery/diesel generator microgrid," Rev. Roum. Sci. Techn. – Électrotechn. Et Énerg., **70**, *4*, pp. 447–452 (2025).
3. E. Bouchetob, B. Nadji, "Deep learning and WBG devices combining to improve PV system efficiency: ANFIS-based MPPT controller," Rev. Roum. Sci. Techn. – Électrotechn. Et Énerg., **70**, *4*, pp. 453–458 (2025).
4. A. Seddjar, K.D.E. Kerrouche, F. Arezki, N. Khorchef, "Comprehensive review of maximum power point tracking techniques and proposed fuzzy logic controller of an electrical power system for nano satellites," Rev. Roum. Sci. Techn. – Électrotechn. Et Énerg., **67**, *2*, pp. 123–131 (2022). Available: https://journal.iem.pub.ro/rrst-ee/article/view/120

5. ***Spectrolab Inc., *XTJ Prime triple-junction solar cell data sheet* (2023).
6. ***Sharp Energy Solutions Corp., *IMM3J solar cells datasheet* (2023).
7. ***GomSpace A/S, "NanoPower DSP datasheet," Rev. 3.1, 2024, https://gomspace.com/product/nanopower-dsp/
8. S.V. Martinez *et al.*, "An integrated thermal-electrical model for simulations of battery behavior in CubeSats," Applied Sciences, **11**, *4*, article 1554 (2021).
9. J. Xie, Y.-Z. Li, L. Yang, Y. Sun, "Thermal impact analysis and electric–thermal coupled modeling of photovoltaic/battery space power system with different surface coatings," Aerospace, **10**, *1*, article 12 (2023).
10. P. Casado, C. Torres, J.M. Blanes, A. Garrigós, D. Marroquí, "Implementation of a 6U CubeSat electrical power system digital twin," Aerospace, **11**, *8*, article 688 (2024).
11. S.A. Khan, A. Ali, M. Tahir, Z. Tao, "Efficient power conditioning: Enhancing electric supply for small satellite missions," Aerospace, **11**, *11*, article 920 (2024).
12. A. Lemmassi, A. Derouich, A. Hanafi, A. Byou, M. Benmessaoud, N. El Ouanjli, "Low-cost MPPT for triple-junction solar cells used in nanosatellites: A comparative study between P&O and INC algorithms," e-Prime – Advances in Electrical Engineering, Electronics and Energy, **7**, article 100426 (2024).
13. M. Noman, U.A. Afzal, I. Ahmad, S. Ahmed, "Modeling and design of power conditioning unit of CubeSat electrical power subsystem with robust nonlinear MPPT controller," ISA Trans., **160**, pp. 150–162 (2025).
14. U. Shakoor, M. Alayedi, E.E. Elsayed, "Comprehensive analysis of CubeSat electrical power systems for efficient energy management," Discover Energy, **5**, article 9 (2025).
15. Z. Mousawi, A. Ali, M.R. Hal, S.A. Khan, A. Egwebe, "Integrated power and attitude sensors tile for a small spacecraft," Results in Engineering, **27**, article 106534 (2025).
16. ***GomSpace A/S, *Nanosatellite platforms*, https://gomspace.com/ (accessed Apr. 23, 2026).
17. ***Airbus, *Eurostar Neo*, https://www.airbus.com/ (accessed Apr. 23, 2026).
18. ***NASA JPL, *ST8 UltraFlex 175*, https://www.jpl.nasa.gov/ (accessed Apr. 23, 2026).
19. ***NASA Webb Telescope Team, *NASA's Webb 'Powerhouse' solar array reconnects to the telescope* (2020).
20. Q.-Y. Liu, Y.-Z. Li, "Thermal stability enhancement of fixed solar panels in nanosatellites based on phase change materials: A thermal-electrical coupling analysis," Appl. Therm. Eng., **284**, article 129189 (2026), https://www.sciencedirect.com/science/article/abs/pii/S1359431125037810.
21. ***NASA Science, *Solar cell and array technologies for future space missions* (2002).
22. M.F. Piszczor, et al., "Advanced solar cell and array technology for NASA deep space missions," Conference Record of the IEEE Photovoltaic Specialists Conference (PVSC) (2008).
23. ***California Polytechnic State University, *CubeSat Design Specification, Rev. 14 (draft),* The CubeSat Program, Cal Poly SLO (2020).
24. ***GomSpace A/S, *NanoPower P110 datasheet, Rev. 2.10* (2018).
25. N.B. Snyder, "Design, validation, and verification of the Cal Poly educational CubeSat kit structure," M.S. thesis, California Polytechnic State University, San Luis Obispo (2020).
26. ***ESA, *100 W Deployable Solar Panels for Nanosatellites* (n.d.; accessed 10 November 2026).
27. H. Taylor, M. Vreugdenburg, L. Sangalli, R. Vincent, "RMCSat: An F10.7 solar flux index CubeSat mission," Remote Sensing, **13**, *23*, article 4754 (2021).
28. N.S. Bennett, A. Hawchar, A. Cowley, "Thermal control of CubeSat electronics using thermoelectrics," Applied Sciences, **13**, *11*, article 6480 (2023).
29. L. Contreras-Benito, K. Osipova, J.N. Buitrago-Leiva, G. Gracia-Sola, F. Coppa, P. Climent-Salazar, P. Sopena-Coello, D. Garcín, J. Ramos-Castro, A. Camps, "3Cat-8 mission: A 6-unit CubeSat for ionospheric multisensing and technology demonstration test-bed," Remote Sensing, **16**, *22*, article 4199 (2024).
30. S.R. Fahim, H.M. Hasanien, R.A. Turky, S.H.E. Abdel Aleem, M. Ćalasan, "A comprehensive review of photovoltaic module models and algorithms used in parameter extraction," Energies, **15**, *23*, article 8941 (2022).
31. R.R. Bate, D.D. Mueller, J.E. White, "Fundamentals of astrodynamics," Dover Publications, New York (1971).
32. D.L. Gerber, et al., "A comprehensive loss model and comparison of AC and DC boost converters," Energies, **14**, *11*, article 3131 (2021).
33. M. Faifer, L. Piegari, M. Rossi, S. Toscani, "An average model of DC–DC step-up converter considering switching losses and parasitic elements," Energies, **14**, *22*, article 7780 (2021).
34. N. Tian, Y. Wang, J. Chen, H. Fang, "One-shot parameter identification of the Thevenin's model for batteries: Methods and validation," J. Energy Storage, **29**, article 101282 (2020).